Journal of Materials Chemistry A

Dual Substitution in Cationic and Anionic Sublattices of Lithium Indium Chloride for High-Performance Solid-State Lithium Metal Batteries

Journal:	*Journal of Materials Chemistry A*
Manuscript ID	TA-ART-03-2025-001706.R1
Article Type:	Paper
Date Submitted by the Author:	15-Apr-2025
Complete List of Authors:	Bahmani, Farzaneh; South Dakota School of Mines and Technology, Materials Engineering & Science program Smirnova, Alevtina; South Dakota School of Mines and Technology, Department of Chemistry, Biology, and Health Sciences, and Materials Engineering and Science program

ARTICLE

Dual Substitution in Cationic and Anionic Sublattices of Lithium Indium Chloride for High-Performance Solid-State Lithium Metal Batteries

Received 00th January 20xx,
Accepted 00th January 20xx

DOI: 10.1039/x0xx00000x

Farzaneh Bahmani,*[a] and Alevtina White Smirnova ,*[a b]

The compatibility of solid-state electrolytes with high-voltage cathodes and their electrochemical stability make them promising candidates for solid-state lithium-metal batteries. Metal-based lithium chlorides were proposed as supersonic conducting electrolytes, however, further enhancements are required regarding their room-temperature ionic conductivity, interfacial stability with lithium metal anodes, and moisture sensitivity. The proposed strategy targets synergistic improvement of these properties by enhancement of the Li_3InCl_6 crystal structure, as a model compound, through dual substitution in its cationic and anionic sublattices. The study reveals that singly doped $Li_3In_{1-x}Zr_xCl_6$ ($0 \le x < 0.6$) electrolytes possess enhanced ionic conductivity, while fluorine-substituted $Li_3InCl_{6-y}F_y$ ($0 \le y < 0.6$) electrolytes have improved oxidation stability at the electrolyte-lithium metal interfaces. The dual substitution results in an optimized $Li_{2.6}In_{0.6}Zr_{0.4}Cl_{5.9}F_{0.1}$ electrolyte with synergistically combined superior properties compared to undoped and single-doped derivatives. The solid-state electrochemical cells with $Li_{2.6}In_{0.6}Zr_{0.4}Cl_{5.9}F_{0.1}$ electrolyte deliver a high specific capacity of 216 mAh g^{-1} at 0.1 C, volumetric energy density of 419.1 Wh cm^{-3}, and gravimetric energy density of 723.3 Wh kg^{-1}. The dual-doping strategy enhances the properties of inorganic solid-state electrolytes, provides critical insights into lithium-ion transport at interfaces, and reveals key transformations in structure-property relationships with progressing from undoped to singly doped, and further to dual-doped superionic conductors for next-generation energy storage systems.

1. Introduction

New energy materials and energy storage technologies have become a critical part of modern research, particularly in the development of solid-state batteries. Compared to conventional lithium-ion batteries with liquid electrolytes, solid-state batteries offer improved safety, thermal stability, and higher energy density in electrochemical cells comprising lithium-metal anodes, solid-state superionic electrolytes, and high-capacity and high-voltage cathodes[1, 2]. Many groups of solid-state electrolytes (SSEs) have been explored, [3, 4] including a broad range of metal-based lithium chlorides (Li_3MCl_6, where the central metal cation M = ^{21}Sc, ^{39}Y, ^{40}Zr, ^{49}In, ^{65}Tb-^{71}Lu, ^{67}Ho, ^{68}Er, ^{70}Yb) with high ionic conductivity and compatibility with high voltage cathodes. [5, 6] However, further enhancements of their ionic conductivity at room temperature, moisture tolerance, and compatibility with lithium-metal anodes are required for adaptation in solid-state battery markets. [7] One of the known approaches for enhancing ionic conductivity involves the aliovalent doping of the central metal cation with other transition metals. This strategy was used to adjust the concentration of charge carriers, expand the interplanar crystal spacing to facilitate ionic transport and create vacancies in ionic sublattices. [8-10] The balance between vacancies and lithium cations defines the efficiency of lithium-ion transport through the crystal lattice. While high-vacancy concentration enhances lithium-ion charge transfer, its excessive concentration reduces the probability of lithium ions accessing neighboring sites and limits the overall solid electrolyte conductivity. [11] Therefore, an optimized dopant concentration was targeted. For instance, high ionic conductivities in Zr-substituted Li_3MCl_6 compounds were achieved by fine-tuning M^{3+} to Zr^{4+} in specific ratios in compounds such as $In(Li_{2.7}In_{0.7}Zr_{0.3}Cl_6)$, [12] $Er(Li_{2.6}Er_{0.6}Zr_{0.4}Cl_6)$, [13] $Yb(Li_{2.7}Yb_{0.7}Zr_{0.3}Cl_6)$, [14] and $Lu(Li_{2.5}Lu_{0.5}Zr_{0.5}Cl_6)$, [15] where the excessive charge from aliovalent Zr^{4+} cations was compensated by certain of lithium vacancies. Another factor that significantly influences both the ionic conductivity and crystal structure is the average size of the central metal cation (M^{3+}). Larger ions favor a trigonal *P3m1* structure (M = Y, Tb-Tm), [13, 16, 17] intermediate-size ions form an orthorhombic *Pnma* structure (M = Yb, Lu), [18] while smaller ions form a monoclinic *C2/m* space group (M= In, Sc). [19, 20] This trend generally holds under similar synthesis conditions; however, minor variations can affect this pattern. [11] For instance, Zr-doping in Li_3MCl_6 (where M = Y, Er, Yb) induces a transition from trigonal to orthorhombic phase, due to the smaller size of Zr (0.72 Å) compared to Y (0.90 Å), Er (0.89 Å), and Yb (0.87 Å). [12, 13] On the contrary, Zr substitution in Li_3InCl_6 does not cause any phase transformations because of similar ionic radii of In^{3+} and Zr^{4+}. This substitution causes only small changes in lattice parameters while maintaining the monoclinic C2/m framework. [11, 14] Therefore, the ionic conductivity enhancement caused by Zr substitution is likely due to changes in the concentration of charge carriers, crystal structure, or diffusion pathways.

Besides obvious benefits, aliovalent substitution can have negative effects by reducing the electrochemical stability window (ESW) as demonstrated earlier for Zr-doped Li_3ErCl_6. [21] While Zr doping improves ionic conductivity, the higher oxidation potential of

[a] *Materials Engineering and Science program, South Dakota Mines, South Dakota 57701, USA. Email:Farzaneh.Bahmani@mines.sdsmt.edu.*
[b] *Department of Chemistry, Biology, and Health Sciences, and Materials Engineering and Science program, South Dakota Mines, South Dakota 57701, USA. Email: Alevtina.Smirnova@sdsmt.edu.*

Supplementary Information available: See DOI: 10.1039/x0xx00000x

Zr^{4+} compared to Er^{3+} leads to a decrease in the electrochemical stability window. To minimize the negative effect of cationic doping, an isovalent anionic substitution was proposed. Specifically, to enhance the oxidation stability of electrolytes in contact with the lithium-metal anode, fluorine atoms were incorporated into halogen sites of Li_3MX_6 (X=Cl, Br, I). However, this substitution resulted in strong Li-F interactions because of the high electronegativity of fluorine, limiting the overall lithium-ion conductivity. [22] In contrast, the partial substitution of bromine by fluorine in $Li_3YBr_{5.7}F_{0.3}$ demonstrated positive effects such as improved ionic conductivity. [23] Furthermore, enhanced ionic conductivity and moisture tolerance, reduced surface defects, and low electronic conductivity were found for fluorine-doped $Li_3InCl_{5.8}F_{0.2}$ compound. [24] One more study revealed that the fluorine incorporation in Li_3InCl_6 ($Li_3InCl_{5.5}F_{0.5}$) resulted in decreased conductivity, but it also expanded the electrochemical stability window and improved overall electrochemical performance. [25] Enhancement of oxidation stability without deterioration of ionic conductivity was observed for fluorine-substituted $Li_3YCl_{5.97}F_{0.03}$. [26]

Compared to aliovalent doping, isovalent substitution enhances the SSE compatibility with lithium metal anodes and prevents lithium dendrite growth during continuous charge-discharge cycles. Regarding the Li_3InCl_6/Li interface, experimental and *ab initio* studies reveal chemical, electrochemical, and thermodynamic instability at this interface. Specifically, Li_3InCl_6/Li interface deterioration arises from a reduction of Li_3InCl_6 and interfacial chemical reactions with lithium metal anode. Since Li_3InCl_6 has a relatively high reduction potential of 2.47 V (*vs*. Li/Li^+), [27] it undergoes reduction during battery charging, leading to increased interfacial resistance [28] and the formation of various redox by-products. At low voltages, Li_3InCl_6 undergoes some consecutive reduction steps, forming LiCl and $InCl_2$ at <2.47 V, [28] In_7Cl_9 at < 2.26 V, LiCl and InCl at <2.18, and, finally, through Li-In alloying $Li_{13}In_3$ at 0.11 V. At higher voltages above 4.34 V, Li_3InCl_6 experiences oxidation via electrochemical de-lithiation and formation of $InCl_3$ and Cl_2 ($Li_3InCl_6 \rightarrow 3Li + InCl_3 + 3/2\ Cl_2$). Fluorine doping in Li_3InCl_6 ($Li_3InCl_{5.5}F_{0.5}$) improved electrochemical cell performance cycled to upper cut-off voltages of 4.5 and 4.8 V (*vs*. Li/Li^+). Generation of stable $LiInF_4$ phase in the $LiNi_{0.7}Mn_{0.2}Co_{0.1}O_2$-$Li_3InCl_{5.5}F_{0.5}$ cathode mixture resulted in the initial discharge capacity of 218.9 mAh g^{-1} and 80.0% capacity retention after 100 cycles in the range of 3.0-4.5 V (*vs*. Li/Li^+). [26] Similar to liquid electrolytes, SSEs form solid electrolyte interface (SEI) layers, especially in the presence of electronegative atoms like fluorine, that have strong binding energy with lithium cations and force them to distribute evenly at the electrolyte/anode interface. Numerous metal alloys and oxides, nitrides, oxy-nitrides, phosphates, carbonates, chlorides, and fluorides have been used to buffer the volumetric expansion of lithium anode, transport lithium cations, and block electron transport. Fluorine-substituted lithium indium halides can serve as a source of lithium fluoride or indium fluoride protective layers, especially at low voltages (<2.47 V). [28] Lithium fluoride, in particular, is known to form natural SEI layers from the decomposition of $LiPF_6$-based liquid electrolyte [29] and minimize the formation of lithium dendrites due to its wide electrochemical stability window, high electron-tunneling barrier, [30] and lipophilic nature. [31]

Besides ionic conductivity and electrochemical stability, moisture tolerance of solid-state electrolytes is another critical aspect that hinders their economic viability in solid-state batteries. Currently, Li_2ZrCl_6 is considered one of the promising SSEs, however, it exhibits only 5 % relative humidity (RH) tolerance [32] and suffers from hygroscopic irreversibility. Moisture tolerance improvements were achieved by considering that soft acids, such as tin (Li_4SnS_4), arsenic ($Li_{3.833}Sn_{0.833}As_{0.166}S_4$), [33] or indium ($Li_3InCl_6$) [34] do not react with water as a hard base. Thermodynamic screening for moisture sensitivity in sulfur-based SSEs reveals that In^{3+}-based compounds are moisture-tolerant [35] and can be dehumidified to restore their original crystal structure by heat treatment. [36] Improvement of $Li_{2+x}Zr_{1-x}In_xCl_6$ ($0.8 \le x \le 1$) hygroscopic reversibility was achieved by the incorporation of soft acid indium into Zr-based chloride as a dopant. [37] The HSAB theory predicts lattice expansion and formation of hydrates (e.g. $Li_3InCl_6{\cdot}2H_2O$), which can reduce the migration energy barrier of lithium ions and offer a reversible hydration/dehydration pathway. This hypothesis was tested for electrochemical cells with $Li_{2.8}Zr_{0.2}In_{0.8}Cl_6$ electrolyte, single-crystal $LiNi_{0.8}Mn_{0.1}Co_{0.1}O_2$ cathode, and Li-In anode. After exposure to humidity and reheating, the cell exhibited 71% capacity retention after 500 cycles at 1 C-rate at 25°C. [37]

Dual substitution has been previously applied to garnet electrolytes, [38] oxide, sulfide, phosphide-based SSEs, [39-41], and cathode materials. [42] Based on this and other data regarding aliovalent and isovalent substitution, this study is focused on dual substitution in lithium indium halide SSEs to synergistically improve major parameters, such as ionic conductivity, moisture tolerance, electrochemical stability, and reduction stability at interfaces with lithium-metal anodes. A comparative analysis of lithium-ion transport and structure-property relationships in the undoped and single-doped Li_3InCl_6 electrolytes with their doubly substituted derivatives provides essential insight into the fundamental properties of solid-state inorganic electrolytes. Co-substitution with zirconium and fluorine atoms results in the innovative superionic conductor for application in next-generation solid-state energy storage.

2. Experimental Section

2.1. Synthesis and materials characterization

To synthesize zirconium- and fluorine-substituted Li_3InCl_6 electrolytes, inorganic precursors, such as LiCl (99.98%, Sigma Aldrich), $InCl_3$ (99.99%, Sigma Aldrich), $ZrCl_4$ (99.95%, Sigma Aldrich), and LiF (99.99%, Sigma Aldrich) were mixed in stoichiometric ratios according to chemical compositions of Li_3InCl_6, $Li_3In_{1-x}Zr_xCl_6$ ($0 \le x < 0.6$), $Li_3InCl_{6-y}F_y$ ($0 \le y < 0.6$), and $Li_{3-x}In_{1-x}Zr_xCl_{6-y}F_y$ ($x = 0.4$ and $y = 0.1$) and ball-milled at 600 rpm for 24 hours in reverse mode (15 min run, 15 min break for cooling) in ZrO_2 jars with ZrO_2 balls (5 and 10 mm in diameter). The ball-milled powders were placed in a Schlenk tube under an Ar atmosphere, sealed, and annealed at 260 °C for 2 hrs at a heating rate of 5 °C min^{-1} in vacuum. The annealed powders were cooled in a vacuum and used for further analysis. The synthesized electrolytes were analyzed by X-ray Diffraction (XRD) using the Empyrean diffractometer from Malvern PANalytical (XRD, Co Kα λ = 1.78899 Å). The XRD spectra were performed in air-tight sample holders with Kapton polyimide film. The XRD Rietveld refinement was performed using CrystalDiffract software. The schematic view of electrolyte crystal structures was created using a 3D visualization program VESTA. The electrolyte morphology and chemical composition were characterized with a DualBeam Helios 5CX scanning electron microscope (SEM) from ThermoFisher Scientific equipped with an energy dispersive spectrometer (EDS). X-ray Photoelectron Spectroscopy (XPS) was performed using a Thermo Fisher Scientific Nexsa G2 system with a monochromatic Al Kα source (1486 eV). The water absorption behavior of the electrolytes was evaluated using TGA/DSC (SDT Q600 V20.9 Build 20) and Nicolet Apex Fourier-transform infrared (FTIR) spectrometer.

2.2. Electrochemical measurements

The SSE ionic conductivity and activation energy at different temperatures were determined using Electrochemical Impedance Spectroscopy (EIS) with ion-blocking symmetric cells. The SSE powders were cold pressed between two stainless steel (SS) disks in a PEEK mold (12 mm diameter) at 260 MPa using a hydraulic press. The EIS measurements were performed using the Solartron 1260 analyzer in the frequency range of 0.3 MHz to 1.0 Hz at 20-70 °C with 20 mV potential amplitude. Humidity tolerance was evaluated by exposing electrolyte powders to air with 14% relative humidity (RH) for a duration of 1, 3, and 5 hrs, followed by ionic conductivity measurements at room temperature (RT). The ionic conductivity (σ) was determined using the following formula:

$$\sigma = \frac{d}{R\,S} \quad (1)$$

Where d is the thickness (cm), S is the area of the pellet (cm^2), and R is electrolyte resistance (Ohm). The activation energy (E_a) was calculated from Arrhenius equation: [43]

$$\sigma = A \exp\left(\frac{-E_a}{k_B T}\right) \quad (2)$$

where σ is ionic conductivity (S cm^{-1}), k_B is Boltzmann constant (J/K), A is Arrhenius pre-exponential factor (s^{-1}), and T is temperature (K).

The electronic conductivity of the solid-state electrolytes was assessed using direct current (DC) polarization in symmetrical cells (SS|SSE|SS) from 0.3 to 2 V for 3 hours. The electronic conductivity at each voltage was determined using Ohm's law:

$$\sigma = \frac{I\,L}{E\,S} \quad (3)$$

where σ is electronic conductivity (S cm^{-1}), L is SSE thickness (cm), S is SSE surface area (cm^2), E is applied voltage (V), and I is current (A).

The SSE electrochemical stability at RT was evaluated from cyclic voltammetry (CV) with asymmetric cells (SS|SSE|LPSC|Li-In) at a scan rate of 0.1 mV/s from 0.05 V to 5.0 V using the BioLogic potentiostat CHI604E. The Li_6PS_5Cl (LPSC) intermediate layer was used to mitigate possible side reactions between the halide SSE and Li-In alloy. The full-cell electrochemical performance was measured with cathodes containing $LiNi_{0.8}Mn_{0.1}Co_{0.1}O_2$ (NMC811, 68 wt.%), SSE (30 wt.%), and CB (2 wt.%). To assemble NMC811-SSE-CB|SSE|LPSC|Li-In cell, SSE powder (70 mg) was put into a PEEK mold and cold-pressed at 216 MPa for 10 min. Then, LPSC powder (30 mg) was added to one side of the SSE pellet, followed by cold pressing at 216 MPa for 10 min. Subsequently, a thin layer of the composite cathode powder (8 mg) was dispersed on the other side of the SSE pellet and cold-pressed at 286 MPa for 10 min. Finally, an indium foil disk (12 mm diameter, 0.1mm thick) was placed on the LPSC surface with a lithium disk (6 mm diameter, 0.1mm thick) on top. Galvanostatic charge-discharge experiments were performed using Arbin battery test station C2001A in the voltage range of 2.5-4.2 V vs. Li/Li^+. Before and after cycling, the assembled cells were evaluated by EIS at RT within a frequency range of 0.3 MHz to 1 Hz and 20 mV amplitude.

3. Results and Discussion

The crystal structures and chemical composition of the undoped Li_3InCl_6 compound and its substituted derivatives were confirmed by XRD (Fig. 1). All diffraction patterns of the Li_3InCl_6, Zr-doped $Li_3In_{1-x}Zr_xCl_6$ ($0 \le x < 0.6$), F-substituted $Li_3InCl_{6-y}F_y$ ($0 \le y < 0.6$), and Zr/F co-doped $Li_{3-x}In_{1-x}Zr_xCl_{6-y}F_y$ (x = 0.4 and y = 0.1) electrolytes correspond to the pure monoclinic crystal phase with C2/m space group (ICCD No. 04-009-9027). The diffraction peaks of Zr-doped Li_3InCl_6 gradually shift toward higher 2θ angles with increasing Zr concentration (Fig. 1a-c), which is attributed to smaller ionic radii of

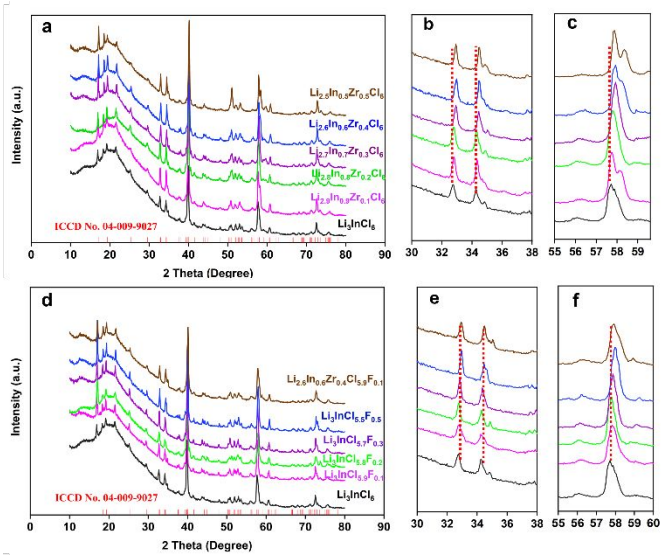

Fig. 1 (a-c) The XRD patterns of Zr-doped $Li_{3-x}In_{1-x}Zr_xCl_6$ ($0 \le x < 0.6$) electrolytes and the corresponding high-resolution 2θ regions. (d-f) The XRD patterns of fluorine-substituted $Li_3InCl_{6-y}F_y$ ($0 \le y < 0.6$) and co-doped $Li_{2.6}In_{0.6}Zr_{0.4}Cl_{5.9}F_{0.1}$ electrolytes and the corresponding high-resolution 2θ regions.

Zr^{4+} (72 pm) compared to In^{3+} (79 pm). According to Bragg's law, the positive shift in 2θ values indicates a reduction in lattice parameters and the formation of short-range ordered structures, [44] which are characteristic of glass or glass-ceramic solid-state electrolytes. [45] This observation is further confirmed by the contraction of the unit cell volume as revealed through Rietveld refinement (Fig. S1). The lattice parameters and the unit cell volume (V) for the optimized Zr-doped $Li_{2.6}In_{0.6}Zr_{0.4}Cl_6$ are smaller (*a*= 6.4014 Å, *b* = 11.0771 Å, *c* = 6.3467 Å and V = 423.32 $Å^3$) compared to pure Li_3InCl_6 (*a* = 6.4079Å, *b* = 11.0795Å, *c* = 6.3824Å, V= 426.40$Å^3$). It is evident that the unit cell contraction primarily affects the *c*-axis of the unit cell, while the *a* and *b* lattice parameters remain unchanged. A similar trend is observed earlier for Zr-doped Li_3InCl_6. [12, 17] Similar to Zr-doping in Li_3InCl_6, fluorine substitution demonstrated a similar unit cell contraction. The diffraction peaks of $Li_3InCl_{6-y}F_y$ ($0 \le y < 0.6$) shift to higher 2θ angles due to a smaller ionic radius of F^- anions (133 pm) compared to Cl^- (181 pm) (Fig. 1d-f). The Rietveld refinement analysis (Fig. S2) demonstrates that the lattice parameters in $Li_3InCl_{5.9}F_{0.1}$ slightly decrease (*a* = 6.4061 Å, *b* = 11.0901 Å, *c* = 6.3461 Å, and V= 425.50 $Å^3$), indicating the lattice shrinkage. [26, 46] The unit cell contraction becomes more visible with increased concentration of fluoride anions, as observed for $Li_3InCl_{5.5}F_{0.5}$ (*a* = 6.4052 Å, *b* = 11.0619 Å, *c* = 6.3751 Å, and V= 425.07 $Å^3$). Compared to $Li_{2.6}In_{0.6}Zr_{0.4}Cl_6$ and $Li_3InCl_{5.9}F_{0.1}$ electrolytes, diffraction peaks of co-substituted $Li_{2.6}In_{0.6}Zr_{0.4}Cl_{5.9}F_{0.1}$ shows more pronounced shifts towards higher 2θ angles, suggesting the formation of defect structure that lacks long-range order periodicity. A comparison of the unit cell parameters and the cell volume for single and dual substitution is presented in Fig. 2a, b, and S3. The $Li_{2.6}In_{0.6}Zr_{0.4}Cl_{5.9}F_{0.1}$ electrolyte reveals a significant reduction of the unit cell parameters (*a* = 6.3971 Å, *b* = 11.0719 Å, *c* = 6.3336 Å, and V = 422.00 $Å^3$) due to smaller ionic radii of dopants that contribute to a denser and more stable crystal lattice that defines the lithium-ion transport. In a monoclinic framework, lithium ions migrate through a three-dimensional network by hopping between neighbouring octahedral sites via intermediate tetrahedral sites. [47] This migration is vacancy-

mediated and strongly influenced by cation and anion site occupancies. Rietveld refinement (Fig. S1, Fig. 2c, Tables S1–S2) reveals that in the co-doped $Li_{2.6}In_{0.6}Zr_{0.4}Cl_{5.9}F_{0.1}$, Zr^{4+} primarily substitutes In^{3+} at the 4g site, which initially shows a low In occupancy of 0.07. After substitution, the Zr occupancy at this site reaches 0.070, while the In occupancy increases to 0.12. Simultaneously, the In occupancy at the 2a site decreased significantly from 0.889 to 0.394. The Li^+ occupancies at the 4h and 2d sites also decrease to 0.82 and 0.74, respectively, creating lithium vacancies. Additionally, F^- partially replaces Cl^- at the 8j site, with an occupancy of 0.065. A schematic of the crystal structure is shown in Fig. 2d. The generation of lithium vacancies plays a critical role in enhancing ionic conductivity, by providing additional hopping sites for lithium-ion diffusion. Compared to undoped and Zr single-doped compositions, co-doping with Zr and F introduces greater vacancies and structural disorders, which synergistically enhance Li^+ transport within the monoclinic lattice. In undoped Li_3InCl_6, lithium-ion transport is limited due to a larger unit cell and fewer intrinsic vacancies, resulting in moderate ionic conductivity. Single-doped electrolyte shows improved conductivity, but lithium vacancy formation is less than in the co-doped system.

The morphology of the optimized electrolytes produced by aliovalent doping ($Li_{2.6}In_{0.6}Zr_{0.4}Cl_6$), and dual substitution ($Li_{2.6}In_{0.6}Zr_{0.4}Cl_{5.9}F_{0.1}$) was compared with undoped Li_3InCl_6. The corresponding changes in Li_3InCl_6 morphology were derived from SEM and EDS data analysis (Fig. 3). The Li_3InCl_6 images show particles ranging from 0.5 to 2.0 µm. These particles demonstrate a distinct crystal structure with well-defined grain boundaries and poor adhesion between them. Upon doping with zirconium, the particle morphology changes, resulting in smaller, irregularly shaped agglomerates with improved connectivity. These changes result from lattice distortions induced by Zr doping and can significantly enhance lithium-ion transport pathways. Even greater structural disorder with more agglomeration and stronger inter-particle adherence is visible for co-doped $Li_{2.6}In_{0.6}Zr_{0.4}Cl_{5.9}F_{0.1}$ compared to the undoped Li_3InCl_6 and singly doped $Li_{2.6}In_{0.6}Zr_{0.4}Cl_6$ electrolytes. The EDX maps of the co-doped $Li_{2.6}In_{0.6}Zr_{0.4}Cl_{5.9}F_{0.1}$ (Fig. 3d), as well as those for undoped Li_3InCl_6 and singly doped $Li_{2.6}In_{0.6}Zr_{0.4}Cl_6$ (Fig. S4), confirm the homogeneous distribution of all existent atoms.

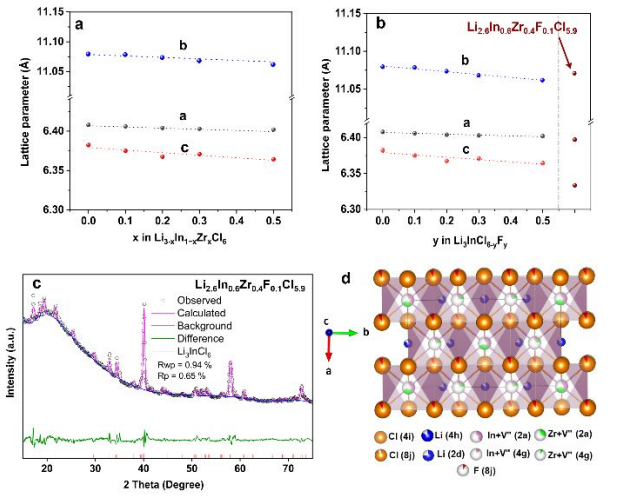

Fig. 2 (a, b) Lattice parameters a, b, and c for Zr-doped $Li_3In_{1-x}Zr_xCl_6$, F-substituted $Li_3InCl_{6-y}F_y$ and co-doped $Li_{2.6}In_{0.6}Zr_{0.4}F_{0.1}Cl_{5.9}$. (c) XRD patterns and Rietveld refinement data for the $Li_{2.6}In_{0.6}Zr_{0.4}Cl_{5.9}F_{0.1}$ electrolyte. (d) Schematic of $Li_{2.6}In_{0.6}Zr_{0.4}Cl_{5.9}F_{0.1}$ crystal structure from Rietveld refinement.

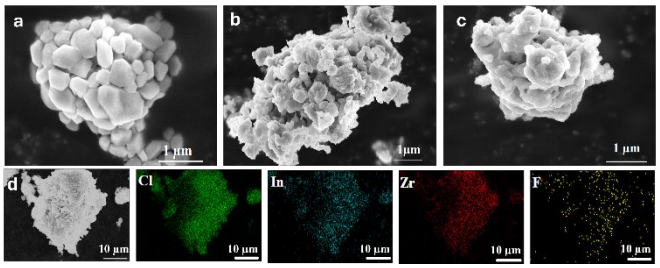

Fig. 3 (a-c) SEM images of undoped Li_3InCl_6, singly doped $Li_3In_{2.6}Zr_{0.4}Cl_6$, and co-doped $Li_{2.6}In_{0.6}Zr_{0.4}Cl_{5.9}F_{0.1}$ electrolytes, respectively. (d) An electron image with the corresponding EDS maps for Cl, In, Zr, and F atoms in $Li_{2.6}In_{0.6}Zr_{0.4}Cl_{5.9}F_{0.1}$ electrolyte.

Impedance spectroscopy served as a tool to observe the structure-property transformations and lithium-ion transport mechanism, focusing on the electrochemical properties of the doped compound $Li_{2.6}In_{0.6}Zr_{0.4}Cl_6$, $Li_3InCl_{5.9}F_{0.1}$, $Li_{2.6}In_{0.6}Zr_{0.4}Cl_{5.9}F_{0.1}$ in comparison to the baseline Li_3InCl_6. The EIS data for Li_3InCl_6 and its doped derivatives in the temperature range of 20−70 °C are presented in Fig. S5 and S6. The Nyquist plot of Li_3InCl_6 shows a visible semicircle at high frequencies, indicating the combined resistance of the bulk material and grain boundaries. At lower frequencies, Warburg response is observed due to non-uniform concentration gradients and non-ideal diffusion to the ion-blocking SS surfaces. The semicircle decreases as temperature rises, which indicates the reduction of grain boundary resistance and enhancement of ionic conductivity. Fig. 4a compares the Nyquist plots of $Li_{3-x}In_{1-x}Zr_xCl_6$ ($0 \le x < 0.6$) at 20 °C. In $Li_{3-x}In_{1-x}Zr_xCl_6$ ($0 \le x < 0.6$), the ionic conductivity increases with Zr concentration up to 0.4, reaching a maximum value of 1.84 mS cm^{-1} which is 2.4-fold higher than that of undoped Li_3InCl_6 (0.77 mS cm^{-1}) and the lowest activation energy of 0.243 eV (Fig. 4b, c). This improvement is caused by the increased number of Li-vacancies and higher crystal structure disorder in $Li_{2.6}In_{0.6}Zr_{0.4}Cl_6$ due to the substitution of In^{3+} with high-valence Zr^{4+} ions. However, a higher concentration of Zr^{4+} ($x = 0.5$) in the indium sublattice interferes with the required level of cation disorder for Li-ion migration and reduces the ionic conductivity. The Nyquist and corresponding Arrhenius plots for F-substituted $Li_3InCl_{6-y}F_y$ and Zr/F co-doped $Li_{2.6}In_{0.6}Zr_{0.4}Cl_{5.9}F_{0.1}$ electrolytes are shown in Fig. 4d-f. In the case of F-substituted $Li_3InCl_{6-y}F_y$ electrolytes, the highest ionic conductivity of 0.81 mS cm^{-1} and the lowest activation energy of 0.246 eV is obtained for $Li_3InCl_{6-y}F_y$ at $y = 0.1$. At the higher concentration of fluorine atoms ($0.2 \le y \le 0.5$), the ionic conductivity decreases due to the high electronegativity of F^- anions which form strong bonds with Li^+ cations and restrict their mobility. Based on these findings, a solid-state electrolyte $Li_{2.6}In_{0.6}Zr_{0.4}Cl_{5.9}F_{0.1}$ with an activation energy of 0.24 eV, and ionic conductivity of 1.72 mS cm^{-1} was selected for further investigation of the aliovalent and isovalent substitution on the electrochemical cell performance. To verify the selection of the co-doped composition, we synthesized and evaluated the room-temperature ionic conductivities of $Li_{2.7}In_{0.7}Zr_{0.3}Cl_{5.9}F_{0.1}$ and $Li_{2.7}In_{0.7}Zr_{0.4}Cl_{5.9}F_{0.2}$ (Fig. S7). However, both exhibited lower conductivity than $Li_{2.6}In_{0.6}Zr_{0.4}Cl_{5.9}F_{0.1}$, indicating that the selected formula provides the optimal balance between cation disorder and anion substitution effects.

The observed ionic conductivity of $Li_{2.6}In_{0.6}Zr_{0.4}Cl_6$ and dual-substituted $Li_{2.6}In_{0.6}Zr_{0.4}Cl_{5.9}F_{0.1}$ electrolyte is higher than previously reported substituted halide electrolytes listed in Table 1. It should be noted that the Arrhenius plot of ionic conductivity versus temperature for all unsubstituted, substituted Li_3InCl_6 electrolytes

exhibits good linearity, indicating no phase transition or ordering change within this temperature range.

Moisture tolerance plays a critical role in solid electrolyte storage and cell fabrication. owever, most halide electrolytes decompose when exposed to ambient air (RH)[8, 16]. The phase evolution of the optimized Li_3InCl_6, $Li_{2.6}In_{0.6}Zr_{0.4}Cl_6$, and $Li_{2.6}In_{0.6}Zr_{0.4}Cl_{5.9}F_{01}$ electrolytes was analyzed after exposure of the powders to air at 15% RH for durations of 1, 3, and 5 hours. In the case of Li_3InCl_6 and $Li_{2.6}In_{0.6}Zr_{0.4}Cl_6$, additional peaks were detected after 3 hrs, whereas $Li_{2.6}In_{0.6}Zr_{0.4}Cl_{5.9}F_{0.1}$ does not show any new peak under the same conditions (Fig. 5a-c). These peaks correspond to the hydrated $Li_3InCl_6{\cdot}xH_2O$ intermediate as further confirmed by the lack of XRD signals of LiCl and $LiCl{\cdot}H_2O$ in the XRD patterns of Li_3InCl_6 after exposure to a humid atmosphere (Fig. S8). The primary diffraction peaks for all materials are indexed to the pristine monoclinic structure of Li_3InCl_6, while the reduced intensity of certain peaks is attributed to surface interactions with moisture. Furthermore, reheating the sample restores their XRD patterns and confirms reversible conversion between Li_3InCl_6 and its hydrate intermediate, similar to $Li_3InCl_6{\cdot}2H_2O$, [20, 34] $Cs_2InCl_5{\cdot}H_2O$, [48] and $Rb_2InCl_5{\cdot}H_2O$ [48] hydrate phase. This behavior is strongly influenced by higher indium concentrations, as observed in $Li_3Y_{1-x}In_xCl_6$ SSEs ($x > 0.5$), where $Li_3Y_{1-x}In_xCl_6{\cdot}xH_2O$ intermediates form instead of phase separation into $LiCl{\cdot}H_2O$ and $YCl_3{\cdot}6H_2O$, which occurs in Li_3YCl_6. [36] These observations highlight the effectiveness of Zr and F doping in enhancing the material's resistance to moisture-induced degradation.

The FT-IR analysis provides further evidence of water absorption (Fig. 5d). In the case of pristine Li_3InCl_6, the intensity of the absorption bands at 3500 cm^{-1} (O–H stretching) and 1500 cm^{-1} (H–O–H bending) progressively increases with exposure time, corresponding to the increase of absorbed moisture. [49] In contrast, Zr-doped $Li_{2.6}In_{0.6}Zr_{0.4}Cl_6$ and Zr-F co-doped $Li_{2.6}In_{0.6}Zr_{0.4}Cl_{5.9}F_{0.1}$ exhibit significantly lower peak intensities, demonstrating their enhanced resistance to moisture uptake compared to undoped Li_3InCl_6, consistent with the XRD results. In addition, TGA analysis for all samples after 5 hours of exposure (Fig. S9) reveals weight loss trends below 150 °C. The total weight loss for Li_3InCl_6 is approximately 2.5%, corresponding to the removal of absorbed water. The overall water loss for Zr-doped and co-doped samples is lower than that of undoped Li_3InCl_6, attributed to the evaporation of surface water.

The enhanced moisture resistance in the Zr- and F-doped samples can be attributed to several factors. The substitution of In^{3+} with smaller and higher-valence Zr^{4+} ions leads to a contraction lattice parameter, as confirmed by the Rietveld refinement, which reduces moisture penetration. Furthermore, the stronger ionic interactions between Zr^{4+} and Cl^- ions also inhibit the hydrolysis process, more prominent in undoped Li_3InCl_6 due to the relatively weaker M–Cl bonds. Additionally, the incorporation of highly electronegative F^- anions further stabilizes the structure by forming shorter and stronger M–F bonds, making the material more resistant to moisture-induced degradation. The strategy of F^- doping and the co-doping of Zr, F to enhance moisture resistance has also been demonstrated in other halide electrolytes, such as $Li_3InCl_{6-x}F_x$ [25, 50] and $Li_{2.4}Y_{0.4}Zr_{0.6}Cl_{5.8}F_{0.15}$. [46]

The EIS data for these samples revealed an increase in resistance with time and a decline in ionic conductivity (Fig. 5d and S10). After exposure to humid air, the Li_3InCl_6 ionic conductivity decreases by 61.9% (from 0.78 to 0.29 mS cm^{-1}), while the conductivity drops for $Li_{2.6}In_{0.6}Zr_{0.4}Cl_6$ is 38.0% (from 1.84 to 1.14 mS cm^{-1}). In contrast, $Li_{2.6}In_{0.6}Zr_{0.4}Cl_{5.9}F_{0.1}$ exhibits a smaller conductivity reduction (from 1.7 to 1.15 mS cm^{-1}) with superior Li-ion conductivity retention of 32.3% due to strong electrostatic interaction between Li-F, Li-Zr, and In-Zr. [51]

The electronic conductivity of Li_3InCl_6, $Li_{2.6}In_{0.6}Zr_{0.4}Cl_6$, and $Li_{2.6}In_{0.6}Zr_{0.4}F_{0.1}Cl_{5.9}$ electrolytes was recorded (Fig. S11) at polarization voltages from 0.3 to 2.0 V during 3 hrs for reaching a steady-state maximum current in the two-blocking electrode setup, which serves as an upper limit for electronic conductivity measurements. [53, 54] An increase in electronic conductivity for all electrolytes is observed with rising polarization voltage (Fig. 5e). The electronic conductivity for $Li_{2.6}In_{0.6}Zr_{0.4}Cl_6$, and $Li_{2.6}In_{0.6}Zr_{0.4}F_{0.1}Cl_{5.9}$ are two orders of magnitude lower than conductivity for undoped Li_3InCl_6, contributing to enhanced stability against Li^+ metal. [51]

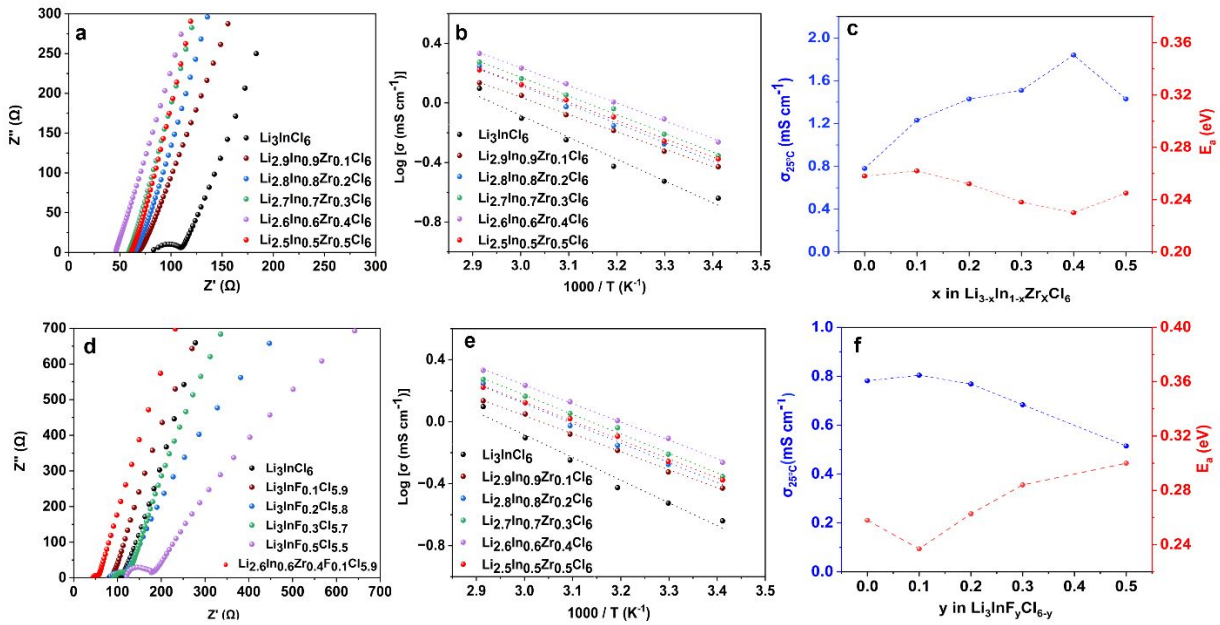

Fig. 4 (a-c) EIS plots at 20 °C, Arrhenius behavior, ionic conductivity, and activation energy for $Li_{3-x}In_{1-x}Zr_xCl_6$ ($0 \le x < 0.6$) electrolytes. (d-f) EIS plots, Arrhenius behavior, ionic conductivity, and activation energy for $Li_3InCl_{6-y}F_y$ ($0 \le y < 0.6$) and $Li_{2.6}In_{0.6}Zr_{0.4}Cl_{5.9}F_{0.1}$ electrolytes.

ARTICLE

Table 1. Comparison of this study with previously reported chloride-based SSEs.

Cell configuration	Ionic conductivity	Initial specific capacity / current density/ coulombic efficiency	Cyclability (retention)	Ref
NMC811-SSE-CB| **$Li_{2.6}In_{0.6}Zr_{0.4}Cl_6$**|LPSC|Li-In NMC811-SSE-CB| **$Li_{2.6}In_{0.6}Zr_{0.4}F_{0.1}Cl_{5.9}$**|LPSC|Li-In	1.84 mS cm^{-1} 1.70 mS cm^{-1}	188.0 mAh g^{-1} (0.1 C) / 95.4 % 216.0 mAh g^{-1} (0.1 C) / 95.9 %	~114 mAh g^{-1} / 50 cycles at 0.1C ~151 mAh g^{-1} / 50 cycles at 0.1C	**This work**
NCM811-SSE-VGNF|**$Li_{2.4}Y_{0.4}Zr_{0.6}Cl_{5.85}F_{0.15}$**|$Li_{5.3}PS_{4.3}ClBr_{0.7}$|Li	1.45 mS cm^{-1}	190 mAh g^{-1} (0.1 C) / 87%	182 mAh g^{-1} / 100 cycles at 0.1 C (95.1%)	7
LCO-SSE-CB|**$Li_{2.9}In_{0.9}Zr_{0.1}Cl_6$**|LGPS|In	1.54 mS cm^{-1}	122.7 mAh g^{-1} (0.1 C) / 99.7%	~65 mAh g^{-1} / 50 cycles at 0.1 C	11
LCO-SSE|**$Li_{2.633}Er_{0.633}Zr_{0.367}Cl_6$**|$Li_3PS_4$|$Li_{11}Sn_6$	1.4 mS cm^{-1}	110 mAh g^{-1} (0.1 C) / 96.4%	~85 mAh g^{-1} / 200 cycle at 0.5C	21
LCO.SSE-VGCF|**$Li_{2.6}Er_{0.6}Zr_{0.4}Cl_6$**|LPSC|Li-In	1.13 mS cm^{-1}	147 mAh·g^{-1} (0.1C) / 97.1%	118 mA g^{-1} / 100 cycle at 0.1C (80%)	13
NMC622| **$Li_{2.7}Yb_{0.7}Zr_{0.3}Cl_6$**| $Li_{6.7}Si_{0.7}Sb_{0.3}S_5I$|Li–In	1.11 mS cm^{-1}	170 mAh g^{-1} (0.2 C) / 97.1%	136 mAh g^{-1} / 150 cycles at 0.2 C (80%)	14
LCO-SSE|**$Li_3InCl_{5.8}F_{0.2}$**|In-Li	1.65 mS cm^{-1}	49.4 mAh g^{-1} (0.05 C) / 86.7%	45.1 mAh g^{-1} / 18 cycles at 0.05C	25
NCM712-SSE|**$Li_3InCl_{5.5}F_{0.5}$**| $Li_{5.5}PS_{4.5}Cl_{1.5}$| Li-In	1.0 mS cm^{-1}	218.9 mAh g^{-1} (0.1 C) / 86.7%	80% / 100 cycles at 0.5C	26
LCO-**$Li_3InCl_{4.8}F_{1.2}$**|Li_3InCl_6|In	0.51 mS cm^{-1}	203.7 mAh g^{-1} (14 mA g^{-1}) / 89.2%	~100 mAh g^{-1} / 70 cycles	52
NMC811-SSE-VGCF|**Mn-doped Li_2ZrCl_6**|Li	0.8 mS cm^{-1}	185.6 mAh g^{-1} (0.1 C) / 94.5 %	88% / 50 cycles at 0.1C	53
LCO-SSE|**Li_2ZrCl_6**|LGePS|Li–In	1.0 mS cm^{-1}	123.4 mAh g^{-1} (0.1 C) / 95.2%	71% / 50 cycles at 0.1C	54
NCM-SSE|**$Li_{2.75}Y_{0.16}Er_{0.16}Yb_{0.16}In_{0.25}Zr_{0.25}Cl_6$**|In/Li–In	1.17 mS cm^{-1}	190 mAh g^{-1} (0.1 C) / 88%	95% / 200 cycles at 0.5 C	55

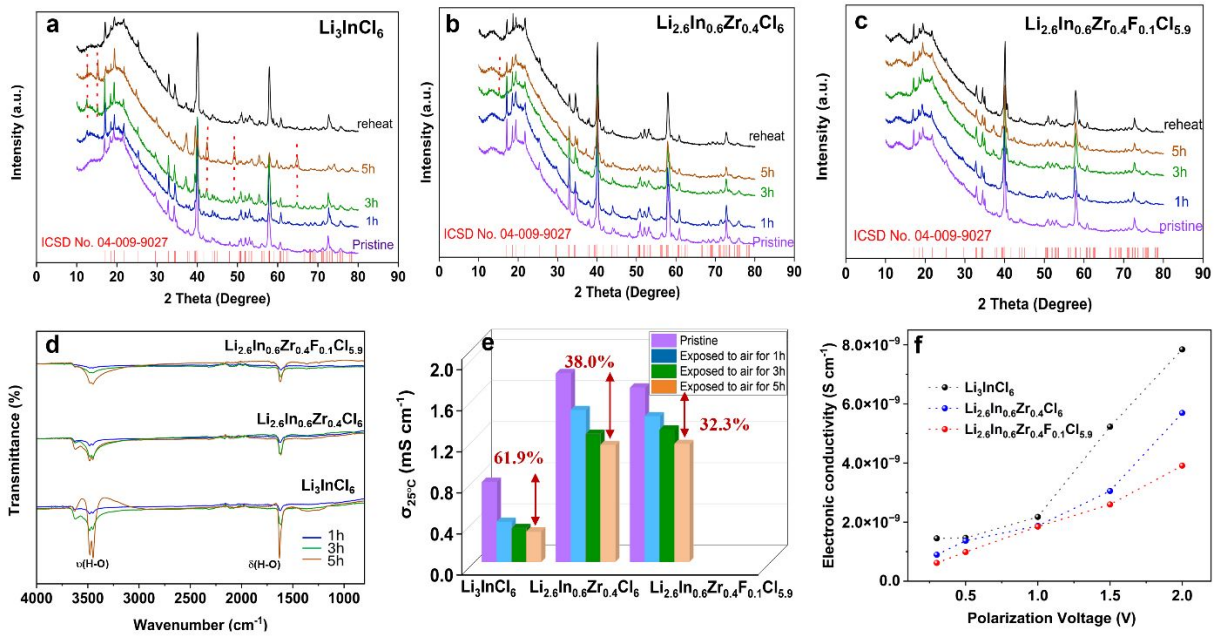

Fig. 5 (a-c) The Phase evolution and (d) Ft-IR spectrum of Li_3InCl_6, $Li_{2.6}In_{0.6}Zr_{0.4}Cl_6$, and $Li_{2.6}In_{0.6}Zr_{0.4}F_{0.1}Cl_{5.9}$ electrolytes exposed to 15% RH air as a function of time. (e) Comparison of the ionic conductivity retention of Li_3InCl_6, $Li_{2.6}In_{0.6}Zr_{0.4}Cl_6$, and $Li_{2.6}In_{0.6}Zr_{0.4}F_{0.1}Cl_{5.9}$ electrolytes after exposure to air for different times. (f) The electronic conductivity of Li_3InCl_6, $Li_{2.6}In_{0.6}Zr_{0.4}F_{0.1}Cl_{5.9}$, and $Li_{2.6}In_{0.6}Zr_{0.4}F_{0.1}Cl_{5.9}$ electrolytes.

ARTICLE

Regarding the electrolyte stability at the interface with the lithium metal anode, the co-doped $Li_{2.6}In_{0.6}Zr_{0.4}Cl_{5.9}F_{0.1}$ exhibited significantly higher stability compared to Li_3InCl_6. The overpotential variation in chloride-based SSE could be due to poor interfacial stability, electrolyte reduction during the plating/stripping process, and SEI instability. [56, 57] In the case of Li_3InCl_6, the initial low plating/stripping overpotential gradually increased to 6.4 V over 590 cycles and then started to decrease reaching 1.47 V, leading to cell short-circuiting (Fig. 6a). The high initial plating/stripping potentials are attributed to interfacial reactions between Lithium and the Li_3InCl_6 SEE while the subsequent decline may indicate the gradual formation of stable interphase and improved contact between lithium and the electrolyte. [50, 57, 58] The overpotential behavior of $Li_{2.6}In_{0.6}Zr_{0.4}Cl_{5.9}F_{0.1}$ exhibits a similar trend with minimal polarization and more stable cycling performance at the same current density. Its initial overpotential increased from 0.32 V to 0.41 V over 50 cycles and then reached 0.06 V over 1400 cycles (Fig. 6b). The superior performance is due to the formation of the LiF interfacial layer. This layer passivates the interface, blocks electron flow while allowing Li-ion transport, and prevents the decomposition of SSE. [44, 59] To investigate the composition of SEI, XPS analysis was performed on cycled $Li/Li_{2.6}In_{0.6}Zr_{0.4}Cl_{5.9}F_{0.1}$ anode (Fig. 6C). In the Li 1s spectrum, a broad peak near 56.9 eV is associated with Lithium in the electrolyte, while a more distinct peak around 54.6 eV indicates the presence of LiF at the interface. [60] The F 1s spectrum shows a peak at around 685 eV, confirming the formation of the LiF-rich interfacial layer. The influence of fluorine on interfacial stabilization was further supported by plating/stripping tests with the highly F-substituted $Li_3InCl_{5.5}F_{0.5}$, which demonstrates a significant reduction in overpotential (Fig. S12), resulting probably from thicker and more stable LiF interfacial layer due to high fluorine concentration.

Regarding the electrochemical stability window derived from CV plots (Fig. 6d-f), Li_3InCl_6 exhibits no peaks in the range of 2-5 V and demonstrates high electrochemical stability. However, Zr-doped $Li_{2.6}In_{0.6}Zr_{0.4}Cl_6$ shows Zr^{4+} oxidation and reduction peaks. This result is consistent with the previous studies indicating that Zr-doping in $Li_{3-x}Er_{1-x}Zr_xCl_6$ [13] and $Li_{2.4}Y_{0.4}Zr_{0.6}Cl_6$ [46] reduces their electrochemical stability. The main reduction peak at 1.7 V can be attributed to the reduction of Zr^{4+} to metallic Zr^0 ($Zr^{4+} + 4e^- \rightarrow Zr$), while the secondary peak below 1.2 V associated with a further reduction of intermediate Zr species ($Zr^{2+} + 2e^- \rightarrow Zr^0$). The oxidation peak at 3.75 V corresponds to the oxidation of metallic Zr back to Zr^{4+} ($Zr^0 \rightarrow Zr^{4+} + 4e^-$). F^- substitution at Cl^- sites extends the electrochemical stability window up to 5.0 V, due to the formation of a stable LiF interphase (Fig. 6c) that protects the interface and suppresses oxidation reactions. [52] This enhancement in electrochemical stability is observed in other halide electrolytes, such as $Li_3InCl_{4.8}F_{1.2}$, [52] $Li_3YBr_{5.7}F_{0.3}$, [44] and $Li_{2.4}Y_{0.6}Zr_{0.4}Cl_{5.8}F_{0.15}$.[46] Increasing the level of F^- substitution can promote the formation of more uniform passivating LiF layers, expanding the oxidation potential to approximately 6.3 V. [23]

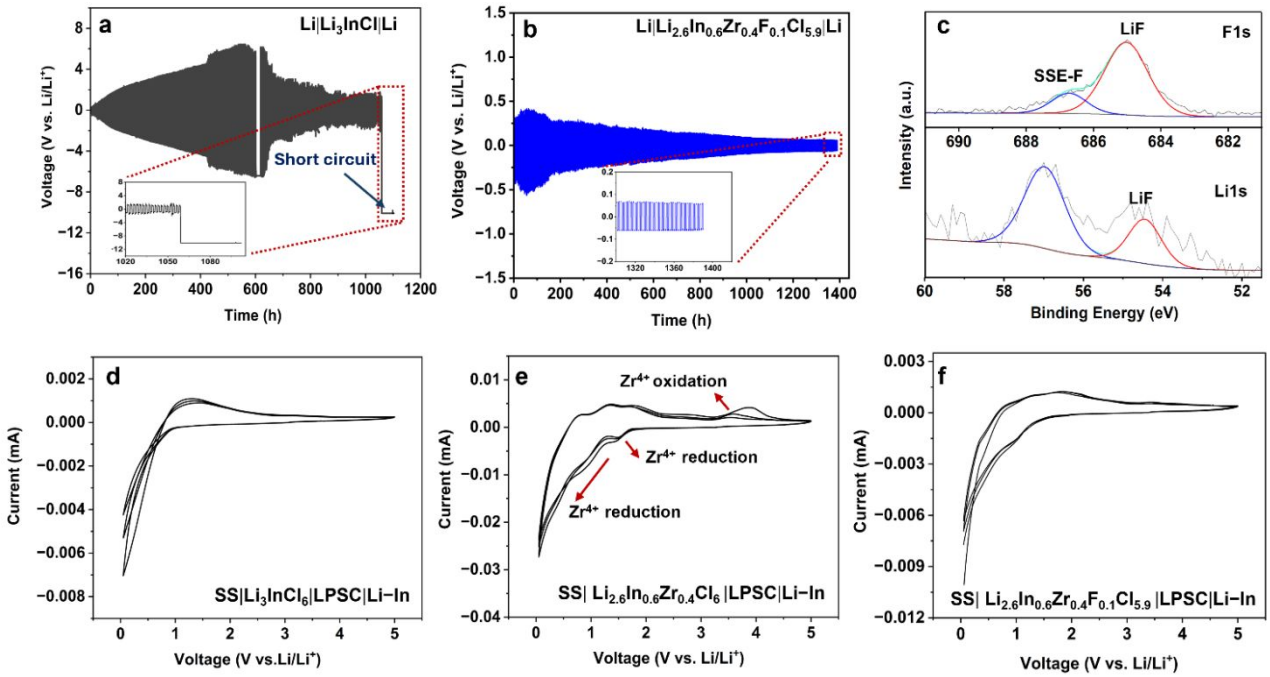

Fig. 6 (a, b) The galvanostatic cycling data for Li|SSE|Li symmetric cells for Li_3InCl_6, $Li_{2.6}In_{0.6}Zr_{0.4}F_{0.1}Cl_{5.9}$, and $Li_3InF_{0.5}Cl_{5.5}$ electrolytes at a current density of 0.05 mA cm^{-2}, respectively. (c) XPS data for the post-mortem analysis of the $Li/Li_{2.6}In_{0.6}Zr_{0.4}F_{0.1}Cl_{5.9}$ anode (d-f) Cyclic voltammetry of SS|SSE|LPSC|Li-In cells for Li_3InCl_6, $Li_{2.6}In_{0.6}Zr_{0.4}Cl_6$, and $Li_{2.6}In_{0.6}Zr_{0.4}F_{0.1}Cl_{5.9}$ electrolytes at a scan rate of 0.1 mVS^{-1}.

ARTICLE

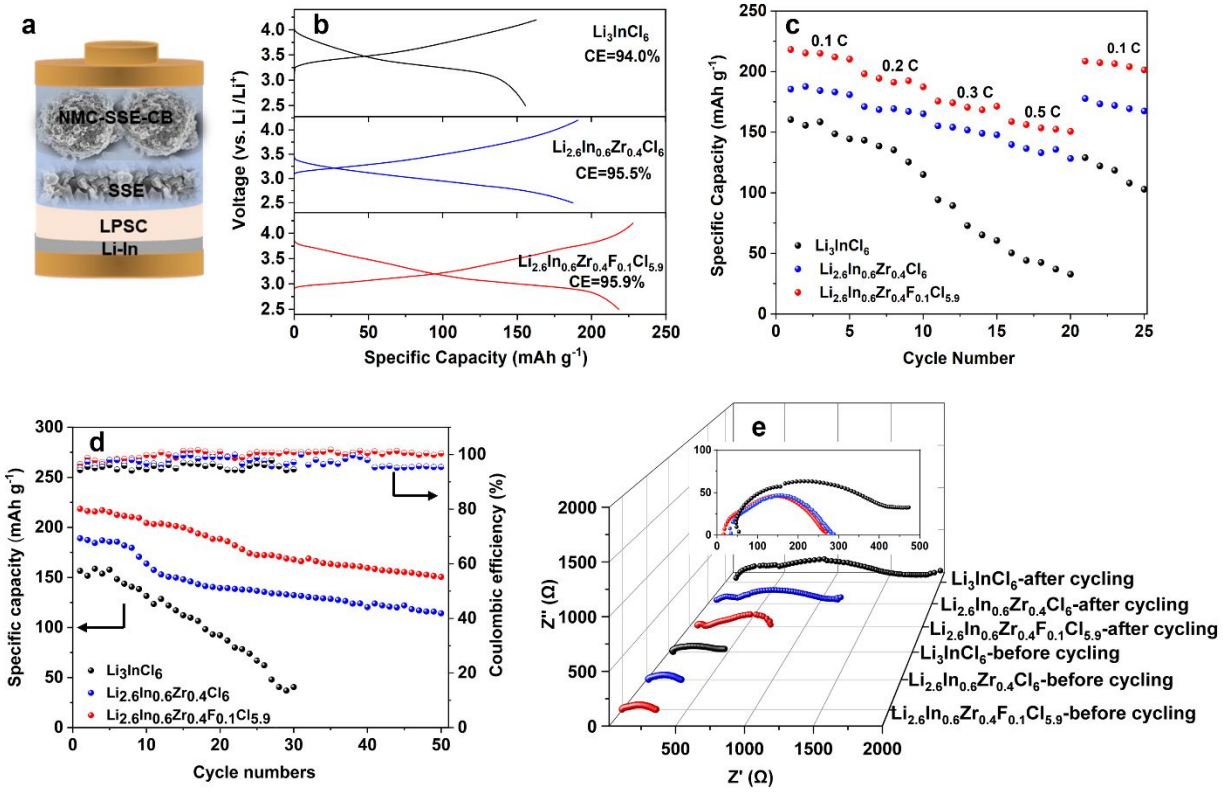

Fig. 7 (a) Schematic representation of NMC-SSE-CB|SSE|LPSC|Li-In solid-state electrochemical cell. The electrochemical performance of the cells with Li_3InCl_6, $Li_{2.6}In_{0.6}Zr_{0.4}Cl_6$, and $Li_{2.6}In_{0.6}Zr_{0.4}Cl_{5.9}F_{0.1}$ electrolytes: (b) Charge-discharge profile at 0.1 C rate, (c) rate capability, (d) cycling stability at 0.1C, (e) EIS plots before and after cycling (Inset: zoomed-in impedance plots before cycling).

The ionic conductivity and oxidation stability of undoped, single-doped, and double-doped electrolytes in electrochemical cells were evaluated with commercial high-voltage NMC811 cathodes. The SEM and EDX data confirm the preservation of NMC811 morphology after grinding, uniform distribution of cathode components, and coverage of NMC811 particles with SSE and CB (Fig. S13). Fig. 7a presents a schematic diagram of the assembled solid-state batteries. The initial charge and discharge profiles for the cells tested at 0.1 C (Fig. 7b) show that the cell with co-doped $Li_{2.6}In_{0.6}Zr_{0.4}F_{0.1}Cl_{5.9}$ delivers an initial discharge capacity of 216 mAh g^{-1}, while $Li_{2.6}In_{0.6}Zr_{0.4}Cl_6$ achieves 188 mAh g^{-1}, with corresponding Coulombic efficiencies (CE) of 95.9% and 95.5%, respectively. These values are higher than those of Li_3InCl_6 (155 mAh g^{-1}, 94.0%), which probably has insufficient ionic transport at the cathode-Li_3InCl_6 electrolyte interface. Compared to other reported solid-state cells the initial efficiency of single-doped electrolytes is higher (Table 1). The cell with a double-doped electrolyte achieved a higher discharge capacity compared to the single-doped $Li_{2.6}In_{0.6}Zr_{0.4}Cl_6$ electrolyte, which is attributed to enhanced ionic conductivity and the formation of a stable Li-ion conductive SEI layer at the interface because of the synergistic effect of aliovalent and isovalent substitution. Rate capability tests demonstrate that $Li_{2.6}In_{0.6}Zr_{0.4}F_{0.1}Cl_{5.9}$ exhibits superior rate capability, delivering specific capacities of 216 mAh g^{-1} at 0.1 C and 158 mAh g^{-1} at 0.5 C, recovering to 208 mAh g^{-1} when the current density returns to its initial value, as shown in Fig 7C and S14. In contrast, $Li_{2.6}In_{0.6}Zr_{0.4}Cl_6$ exhibits a lower capacity of 185 mAh g^{-1} (0.1 C) and declines to 132 mAh g^{-1} (0.5 C), while Li_3InCl_6 demonstrates poor rate capability under the same conditions. The calculated volumetric and gravimetric energy densities of $Li_{2.6}In_{0.6}Zr_{0.4}F_{0.1}Cl_{5.9}$ are 419.1 Wh cm^{-3} and 723.3 Wh kg^{-1}, respectively. The charge-discharge profiles and cyclability data for the cells with double-doped reveal 151 mAh g^{-1} specific capacity after 50 cycles at 0.1 C, which is higher than the corresponding values for $Li_{2.6}In_{0.6}Zr_{0.4}Cl_6$ (114 mAh g^{-1}) (Fig. 7d and S15).

The EIS data was recorded before and after 50 cycles (Fig. 7e). Before cycling, the impedance of the Zr single-doped and Zr/F double-doped cells is nearly the same. The EIS plots show a high-frequency intercept with the x-axis that corresponds to the bulk resistance of the solid-state electrolyte (R_{SSE}), followed by two typical semicircles. The first semicircle is associated with the interface resistance (R_{if}) at the SSE/electrode interface and the halide/LPSC interface, while the second semicircle represents charge transfer

resistance (R_{ct}). The corresponding fitting results of EIS plots after cycling from the equivalent electric circuit are displayed in Table S3.

The increase in resistance after cycling could be attributed to the formation of SEI layers, [61] electrochemical degradation on both anode and cathode sides, [62] and mechanical stress-induced structural changes during cycling. [63] Each of these factors can negatively impact the Li-ion transport pathways and increase the overall cell resistance. The interface between Li_3InCl_6 and the NMC-CB cathode is prone to the formation of resistive interphases and voids, which hinder lithium-ion diffusion and reduce ionic conductivity, leading to a rapid decline in capacity. The SEI layer formed during cycling may thicken and become less conductive, especially on the cathode side due to oxidative decomposition. On the anode side, reactions between lithium and LPSCl, coupled with mechanical strain, can lead to the formation of insulating products such as Li_2S and P_2S_x, which increase the interfacial resistance and compromise long-term performance.[64, 65] Moreover, the continuous formation of SEI layers may consume active lithium, further contributing to an impedance rise.[66]

Doping the electrolyte has proven to be an effective strategy for mitigating such interfacial degradation. The R_{if} of the cell assembled with undoped Li_3InCl_6 is three times higher than that of the single-doped electrolyte, confirming the superior interfacial stability of the aliovalent-substituted electrolyte compared to the Li_3InCl_6 electrolyte. This is due to enhanced ionic conductivity, better interfacial contact, and the formation of an efficient conduction network in the composite cathode. [60] In contrast, a double-doped electrolyte demonstrated a greater reduction in R_{if}, lowering it by approximately 2.5 times compared to the single-doped electrolyte. This significant enhancement in the double-doped electrolyte suggests improved electrode-electrolyte compatibility due to the formation of a passivating interfacial LiF layer that mitigates degradation during cycling. [11]

4. Conclusions

This study highlights significant advancements in solid-state electrolyte development through a fundamental comparative study of an undoped model compound (Li_3InCl_6) with single-doped, and dual-doped solid-state derivatives. The substitution of Zr^{4+} at In^{3+} sites enhanced ionic conductivity by increasing lithium vacancy concentrations and expanding interplanar spacing, which facilitated efficient Li-ion transport, as evidenced by the high ionic conductivity of $Li_{2.6}In_{0.6}Zr_{0.4}Cl_6$ (1.84 mS cm^{-1}). However, this improvement results in a less wide electrochemical stability window. To address this, the isovalent substitution of F^- at Cl^- sites was performed to improve the electrolyte interface by forming a passivating LiF layer moisture tolerance and enhancing moisture tolerance. As a result, the optimized dual-doped $Li_{2.6}In_{0.6}Zr_{0.4}Cl_{5.9}F_{0.1}$ electrolyte demonstrated high conductivity comparable to the single-doped electrolyte (1.7 mS cm^{-1}) but significantly improved its electrochemical stability and moisture resistance. The structure-property relationship reveals that the combination of aliovalent and isovalent substitutions effectively optimizes the electrolyte's performance for solid-state battery applications. The solid-state batteries assembled with NMC811 cathode and $Li_{2.6}In_{0.6}Zr_{0.4}Cl_{5.9}F_{0.1}$ electrolyte deliver an initial discharge capacity of 216 mAh g^{-1} at a 0.1 C rate with high Coulombic efficiency of 95.58%. This dual doping approach provides valuable insights into the mechanisms of lithium-ion transport and shows how the structure-property relationships evolve from undoped to single-doped, and further to dual-doped superionic conductors. This transformation emphasizes the role of doping in enhancing material properties, leading to improved ionic conductivity and electrochemical stability for solid-state battery applications.

Author contributions

Farzaneh Bahmani: Conceptualization, Data curation, Formal analysis, Methodology, Software, Validation, Visualization, Writing – original draft.

Alevtina Smirnova: Funding acquisition, Project administration, Resources, Supervision, Writing– review & editing.

Conflicts of interest

The authors declare that they have no conflict of interest.

Data Availability Statement

The data supporting this article have been included as part of the Supplementary Information.

Acknowledgments

The authors acknowledge financial support from the NSF IUCRC program (Award number 2052631) for supporting the "Centre for Solid-state Electric Power Storage (CEPS)" and the South Dakota "Governor's Research Centre for Electrochemical Energy Storage" from the South Dakota Board of Regents (Award numbers 442274 and 442385).

Notes and references

1. K. Tuo, C. Sun, C. A. Lopez, M. T. Fernández-Díaz and J. A. Alonso, *J. Mater. Chem. A* , 2023, **11**, 15651-15662.
2. A. Baniya, M. B. Saud, H. Li, M. B. Faheem, Y. Zhang, A. Thapa, R. S. Bobba, P. I. Kaswekar and Q. Qiao, *Sustain. Energy Fuels*, 2024, **8**, 3574-3582.
3. J. Huang, C. Li, D. Jiang, J. Gao, L. Cheng, G. Li, H. Luo, Z. L. Xu, D. M. Shin and Y. Wang, *Adv. Funct. Mater.,* 2024, 2411171.
4. T. Zhang, W. He, W. Zhang, T. Wang, P. Li, Z. Sun and X. Yu, *Chem. Sci.*, 2020, **11**, 8686-8707.
5. S. Deng, M. Jiang, N. Chen, W. Li, M. Zheng, W. Chen, R. Li, H. Huang, J. Wang and C. V. Singh, *Adv. Funct. Mater.,* 2022, **32**, 2205594.
6. F. Bahmani, C. Rodmyre, K. Ly, P. Mack and A. White Smirnova, *Batteries*, 2024, **10**, 21.
7. Y. Subramanian, R. Rajagopal and K.-S. Ryu, *ACS Appl. Mater. Interfaces,* 2024.
8. X. Li, J. Liang, X. Yang, K. R. Adair, C. Wang, F. Zhao and X. Sun, *Energy Environ. Sci. ,* 2020, **13**, 1429-1461.
9. J. Park, D. Han, H. Kwak, Y. Han, Y. J. Choi, K.-W. Nam and Y. S. Jung, *Chem. Eng. J.*, 2021, **425**, 130630.
10. K. Tuo, C. Sun, C. López, M. T. Fernández-Díaz and J. A. Alonso, *J. Mater. Chem. A* , 2023, **11**, 15651-15662.
11. X. Luo, X. Wu, J. Xiang, D. Cai, M. Li, X. Wang, X. Xia, C. Gu and J. Tu, *ACS Appl. Mater. Interfaces,* 2021, **13**, 47610-47618.
12. E. van der Maas, T. Famprikis, S. Pieters, J. P. Dijkstra, Z. Li, S. R. Parnell, R. I. Smith, E. R. van Eck, S. Ganapathy and M. Wagemaker, *J. Mater. Chem. A,* , 2023, **11**, 4559-4571.
13. Q. Shao, C. Yan, M. Gao, W. Du, J. Chen, Y. Yang, J. Gan, Z. Wu, W. Sun and Y. Jiang, *ACS Appl. Mater. Interfaces,* 2022, **14**, 8095-8105.

14. S. Y. Kim, K. Kaup, K.-H. Park, A. Assoud, L. Zhou, J. Liu, X. Wu and L. F. Nazar, *ACS Mater. Lett.,* 2021, **3**, 930-938.
15. C. Wang, S. Wang, X. Liu, Y. Wu, R. Yu, H. Duan, J. T. Kim, H. Huang, J. Wang and Y. Mo, *Energy Environ. Sci. ,* 2023, **16**, 5136-5143.
16. T. Asano, A. Sakai, S. Ouchi, M. Sakaida, A. Miyazaki and S. Hasegawa, *Adv. Mater.*, 2018, **30**, 1803075.
17. B. Helm, R. Schlem, B. Wankmiller, A. Banik, A. Gautam, J. Ruhl, C. Li, M. R. Hansen and W. G. Zeier, *Chem. Mater.*, 2021, **33**, 4773-4782.
18. R. Schlem, S. Muy, N. Prinz, A. Banik, Y. Shao-Horn, M. Zobel and W. G. Zeier, *Adv. Energy Mater.*, 2020, **10**, 1903719.
19. A. Bohnsack, F. Stenzel, A. Zajonc, G. Balzer, M. S. Wickleder and G. Meyer, *Zeitschrift für anorganische und allgemeine Chemie*, 1997, **623**, 1067-1073.
20. X. Li, J. Liang, J. Luo, M. N. Banis, C. Wang, W. Li, S. Deng, C. Yu, F. Zhao and Y. Hu, *Energy Environ. Sci. ,* 2019, **12**, 2665-2671.
21. K.-H. Park, K. Kaup, A. Assoud, Q. Zhang, X. Wu and L. F. Nazar, *ACS Energy Lett.*, 2020, **5**, 533-539.
22. L. Zhou, C. Y. Kwok, A. Shyamsunder, Q. Zhang, X. Wu and L. F. Nazar, *Energy Environ. Sci. ,* 2020, **13**, 2056-2063.
23. S. Kim, Y. Lee, K. Kim, B. C. Wood, S. S. Han and S. Yu, *ACS Energy Lett.*, 2023, **9**, 38-47.
24. G. Accardo, A. Orue, D. Chatzogiannakis, P. Gluchowski, M. Casas-Cabanas and P. López-Aranguren, *J. Power Sources*, 2023, **585**, 233632.
25. Q. Wang, X. Ma, Q. Liu, D. Sun and X. Zhou, *J. Alloys Compod*, 2023, **969**, 172479.
26. Z. Jiang, C. Liu, J. Yang, X. Li, C. Wei, Q. Luo, Z. Wu, L. Li, L. Li and S. Cheng, *Chin. Chem. Lett.*, 2024, 109741.
27. C.-M. Wang, C.-H. Hsu, J.-S. Yang and P.-C. Tsai, *arXiv preprint arXiv:2412.02433*, 2024.
28. L. M. Riegger, R. Schlem, J. Sann, W. G. Zeier and J. Janek, *Angew. Chem. Int. Ed.*, 2021, **60**, 6718-6723.
29. J. Ko and Y. S. Yoon, *Thin Solid Films*, 2019, **673**, 119-125.
30. Z. Liu, Y. Qi, Y. Lin, L. Chen, P. Lu and L. Chen, *J. Electrochem. Soci.* 2016, **163**, A592.
31. D. Lin, Y. Liu, W. Chen, G. Zhou, K. Liu, B. Dunn and Y. Cui, *Nano Lett.*, 2017, **17**, 3731-3737.
32. K. Wang, Q. Ren, Z. Gu, C. Duan, J. Wang, F. Zhu, Y. Fu, J. Hao, J. Zhu and L. He, *Nature Commun.*, 2021, **12**, 1-11.
33. G. Sahu, Z. Lin, J. Li, Z. Liu, N. Dudney and C. Liang, *Energy Environ. Sci. ,* 2014, **7**, 1053-1058.
34. X. Li, J. Liang, N. Chen, J. Luo, K. R. Adair, C. Wang, M. N. Banis, T. K. Sham, L. Zhang and S. Zhao, *Angew. Chem.*, 2019, **131**, 16579-16584.
35. Y. Zhu and Y. Mo, *Angew. Chem. Int. Ed.*, 2020, **59**, 17472-17476.
36. X. Li, J. Liang, K. R. Adair, J. Li, W. Li, F. Zhao, Y. Hu, T.-K. Sham, L. Zhang and S. Zhao, *Nano Lett.*, 2020, **20**, 4384-4392.
37. K. Wang, Z. Gu, H. Liu, L. Hu, Y. Wu, J. Xu and C. Ma, *Adv.Sci.*, 2024, **11**, 2305394.
38. Y. Meesala, Y.-K. Liao, A. Jena, N.-H. Yang, W. K. Pang, S.-F. Hu, H. Chang, C.-E. Liu, S.-C. Liao and J.-M. Chen, *J. Mater. Chem. A* , 2019, **7**, 8589-8601.
39. Y. Wang, Y. Wu, Z. Wang, L. Chen, H. Li and F. Wu, *J. Mater. Chem. A,* , 2022, **10**, 4517-4532.
40. Z. Wang, Y. Jiang, J. Wu, Y. Jiang, W. Ma, Y. Shi, X. Liu, B. Zhao, Y. Xu and J. Zhang, *Nano Energy*, 2021, **84**, 105906.
41. A. D. Bui, S.-H. Choi, H. Choi, Y.-J. Lee, C.-H. Doh, J.-W. Park, B. G. Kim, W.-J. Lee, S.-M. Lee and Y.-C. Ha, *ACS Appl. Energy Mater.*, 2021, **4**, 1-8.
42. H. G. Park, K. Min and K. Park, *ACS Appl. Mater. Interfaces,* 2022, **14**, 5168-5176.
43. Z. Li, J. Fu, X. Zhou, S. Gui, L. Wei, H. Yang, H. Li and X. Guo, *Adv. Sci.*, 2023, **10**, 2201718.
44. T. Yu, J. Liang, L. Luo, L. Wang, F. Zhao, G. Xu, X. Bai, R. Yang, S. Zhao and J. Wang, *Adv. Energy Mater.*, 2021, **11**, 2101915.
45. T. K. Pietrzak, M. Wasiucionek and J. E. Garbarczyk, *Nanomater.*, 2021, **11**, 1321.
46. Y. Subramanian, R. Rajagopal and K.-S. Ryu, *ACS Appl. Mater. Interfaces,* 2024, **16**, 24534-24546.
47. C. Wang, J. Liang, J. T. Kim and X. Sun, *Sci. Adv.*, 2022, **8**, eadc9516.
48. E. M. Kartzmark, *Can. J. Chem.*, 1977, **55**, 2792-2798.
49. S. Wang, X. Xu, C. Cui, C. Zeng, J. Liang, J. Fu, R. Zhang, T. Zhai and H. Li, *Adv. Funct. Mater.,* 2022, **32**, 2108805.
50. X. Chen, Z. Jia, H. Lv, C. Wang, N. Zhao and X. Guo, *J. Power Sources*, 2022, **545**, 231939.
51. W. L. Huang, N. Zhao, Z. J. Bi, C. Shi, X. X. Guo, L. Z. Fan and C. W. Nan, *Mate. Today Nano*, 2020, **10**, 100075.
52. S. Zhang, F. Zhao, S. Wang, J. Liang, J. Wang, C. Wang, H. Zhang, K. Adair, W. Li and M. Li, *Adv. Energy Mater.*, 2021, **11**, 2100836.
53. H.-J. Jeon, Y. Subramanian and K.-S. Ryu, *J. Power Sources*, 2024, **602**, 234343.
54. J. Shi, Z. Yao, J. Xiang, C. Cai, F. Tu, Y. Zhang, W. Yao, Q. Jia, Y. Zhou and S. Shen, *ACS Sustain. Chem. Eng.*, 2024, **12**, 2009-2017.
55. Q. Wang, Y. Zhou, X. Wang, H. Guo, S. Gong, Z. Yao, F. Wu, J. Wang, S. Ganapathy and X. Bai, *Nature Commun.*, 2024, **15**, 1050.
56. Y.-C. Yin, J.-T. Yang, J.-D. Luo, G.-X. Lu, Z. Huang, J.-P. Wang, P. Li, F. Li, Y.-C. Wu and T. Tian, *Nature*, 2023, **616**, 77-83.
57. E. Umeshbabu, S. Maddukuri, Y. Hu, M. Fichtner and A. R. Munnangi, *ACS Appl. Mater. Interfaces,* 2022, **14**, 25448-25456.
58. J. Liang, X. Li, S. Wang, K. R. Adair, W. Li, Y. Zhao, C. Wang, Y. Hu, L. Zhang and S. Zhao, *J. Am. Chem. Soc.*, 2020, **142**, 7012-7022.
59. M. Yamagishi, C. Zhong, D. Shibata, M. Morimoto and Y. Orikasa, *Electrochem.*, 2023, **91**, 037002-037002.
60. M. Xin, Z. Liu, Y. Liu, F. Dong, P. Xu, H. Sun, H. Xie and Y. Liu, *Renew.*, 2023, **1**, 591-600.
61. B. Wu, C. Chen, D. L. Danilov, M. Jiang, L. H. Raijmakers, R. d.-A. Eichel and P. H. Notten, *ACS omega*, 2022, **7**, 32740-32748.
62. K. Jia, G. Yang, Y. He, Z. Cao, J. Gao, H. Zhao, Z. Piao, J. Wang, A. M. Abdelkader and Z. Liang, *Adv. Mater.*, 2024, **36**, 2313273.
63. Q. Tu, L. Barroso-Luque, T. Shi and G. Ceder, *Cell Rep. Physic. Sci.*, 2020, **1**, 100106.
64. Q. Zheng, Y. Song, W. Huang, J. Yang, T. Li and Y. Xu, *Energy Storage Mater.*, 2023, **63**, 103038.
65. G. G. Serbessa, B. W. Taklu, Y. Nikodimos, N. T. Temesgen, Z. B. Muche, S. K. Merso, T.-I. Yeh, Y.-J. Liu, W.-S. Liao and C.-H. Wang, *ACS Appl. Mater. Interfaces,* 2024, **16**, 10832-10844.
66. M. Li, S. Yang and B. Li, *Interd. Mater.*, 2024, **3**, 805-834.

Data Availability statements

The data supporting this article have been included as part of the Supplementary Information.